

ANKAphase – software for single-distance phase-retrieval from inline X-ray phase contrast radiographs

T. WEITKAMP,^{a*} D. HAAS,^{b,c} D. WĘGRZYNEK^d AND A. RACK^{a*}

^aEuropean Synchrotron Radiation Facility, F-38043 Grenoble France, ^bInstitute for Synchrotron Radiation (ANKA) – K.I.T., D-76021 Karlsruhe Germany,

^cHochschule Darmstadt (h_da), D-64295 Darmstadt Germany, and ^dInternational Atomic Energy Agency, A-1400 Vienna Austria (current address: University of Science and Technology, 30-059 Krakow Poland). E-mail: tim.weitkamp@synchrotron-soleil.fr, arack@snafu.de

(Received 0 XXXXXXXX 0000; accepted 0 XXXXXXXX 0000)

Phase retrieval, X-ray phase contrast, synchrotron radiation, microtomography, X-ray imaging, Java, ImageJ

Abstract

We present a computer program named ANKAphase that processes X-ray inline phase-contrast radiographs by reconstructing the projected thickness of the object(s) imaged. The program uses a single-distance non-iterative phase-retrieval algorithm described in a paper by David Paganin *et al.* (2002). ANKAphase is designed to be used with tomography data (although it does not perform tomographic reconstruction itself). It can process series of phase-contrast radiographs, and if desired, also performs flatfield and darkfield correction. ANKAphase is written in Java and can either be used as a standalone application or as a plugin to ImageJ, a widely-used scientific image processing program. We give a description of the program and show example applications.

Manuscript dated October 6, 2010.

1. Introduction

Hard X-ray imaging with high spatial resolution is an established analytical tool for investigating specimens in two or three dimensions and in a widely non-destructive manner. Its capabilities can be significantly extended when synchrotron light sources are employed as higher resolution in space and time as well as sophisticated contrast modes become accessible. For a brief introduction into the techniques the reader is referred to the literature, *e. g.*, (Graeff & Engelke, 1991; Stevenson *et al.*, 2003; Banhart, 2008; Stock, 2008).

A simple but powerful approach to access higher imaging sensitivity when using synchrotron light sources is a technique known as X-ray inline phase contrast or propagation-based phase contrast: by leaving an appropriate drift space between the sample and the imaging detector, interfaces within the probed specimen can be visualised. If the X-ray wavefront has a sufficient degree of transverse coherence, Fresnel diffraction on microscale structures will lead to interference fringes that enhance edges and interfaces of the sample in the recorded radiograph (Snigirev *et al.*, 1995; Cloetens *et al.*, 1996; Nugent *et al.*, 1996; Wilkins *et al.*, 1996). Compared to the conventional absorption contrast, X-ray inline phase contrast allows studying objects with either negligible absorption or multi-constituent samples in which the different components show too similar absorption to be discriminated.

In projection radiographs, for structures whose size d fulfils the condition $d \gg \sqrt{\lambda z}$ (where λ is the X-ray wavelength and z the distance between the object and the detector plane), the phase-contrast signal can be approximated as the Laplacian of the wavefront phase profile, $\nabla_{xy}^2 \phi(x, y)$ (where x and y are the Cartesian coordinates in the image and/or object plane). Tomographic reconstruction without phase retrieval yields the three-dimensional distribution of the three-dimensional Laplacian of the decrement of refractive index, $\nabla_{x'y'z'}^2 \delta(x', y', z')$ (where x', y', z' are the Cartesian coor-

dinates in the image and/or object plane) (Weitkamp, 2002). While this information is often useful for visual inspection of the data by a human beholder, any further quantitative analysis that requires segmentation of the tomography volume data is not easily possible using the plain phase-contrast data. This is because the gray levels within the different materials regions are not necessarily different; they are just varying at the interfaces. In other words, there is no direct correlation between the gray level of a voxel and the material or density corresponding to this voxel. Without the use of phase retrieval, complex routines need to be developed and applied to make segmentation possible (Antoine *et al.*, 2002; Socha & De Carlo, 2008). Especially volume image analysis is required in order to derive statistically relevant information or to approach more sophisticated problems like potential spatial cross-correlations between different constituents within the data, cf., *e. g.*, (Zabler *et al.*, 2007; Manke *et al.*, 2007; Stiller *et al.*, 2009; Ohser & Schladitz, 2009; Rack *et al.*, 2009a; Brun *et al.*, 2010).

A variety of phase-retrieval methods for X-ray inline phase contrast data has been developed since the mid-1990s. Some of the proposed methods are iterative (Kohn, 1997; Schelokov *et al.*, 2002), but most use analytical approaches. These non-iterative methods differ in the amount of raw data needed (in particular, many methods require images taken at different distances z), restrictions on sample composition and/or X-ray optical properties of the sample, properties of the X-ray beam, and quality of the reconstruction – in particular, accuracy of the reconstructed phase values and spatial resolution of the results. Published examples are (Maleki & Devaney, 1994; Nugent *et al.*, 1996; Cloetens *et al.*, 1999; Gureyev *et al.*, 1999; Schelokov *et al.*, 2002; Bronnikov, 2002; Paganin *et al.*, 2002; Gureyev *et al.*, 2002; Groso *et al.*, 2006; Langer *et al.*, 2008).

For the software tool presented here, a single-distance phase-retrieval method developed by Paganin *et al.* (2002) was chosen. This particular algorithm was selected

among other methods that retrieve the phase from radiographs taken at a single distance because unlike many of these methods, it does not require the sample to show only negligible absorption. Instead, it assumes that the sample is made of a single material. This means that retrieval of the wavefront phase $\phi(x, y)$ at the sample exit plane is equivalent to retrieval of the projected sample thickness $t(x, y)$, as these two quantities are related to each other by $\phi(x, y) = 2\pi\delta t(x, y)/\lambda$. The algorithm is derived for monochromatic illumination. Further below we shall demonstrate that in practice, Paganin's approach shows substantial tolerance to violation of these two conditions. The method already demonstrated its high potential for specimens from diverse scientific fields (Peele *et al.*, 2005; Ohser *et al.*, 2009; Xu *et al.*, 2010; Mayo *et al.*, 2010; Denecke *et al.*, 2011).

The computer program presented here is a simple but robust tool which runs independent of hardware platform and operating system and has an intuitive graphical user interface. It is our hope that this will make phase sensitive imaging techniques, including phase reconstruction, available to a wider range of synchrotron users. This is of particular interest for scientific fields where excellent volume renderings are required, for example in biology (Westneat *et al.*, 2003; Westneat *et al.*, 2008; Socha *et al.*, 2007). Furthermore, quantitative volume image analysis will become feasible for tomographic images acquired *via* edge enhanced projections without extensive data pre-processing (Antoine *et al.*, 2002; Martín-Herrero & Germain, 2007). Data taken in the past without any original intent of phase retrieval may be re-visited for phase reconstruction. Finally, X-ray inline phase contrast being accessible under moderate coherence conditions and even with polychromatic radiation, semi-quantitative phase-sensitive imaging becomes possible at a broader range of synchrotron light sources (Peele *et al.*, 2005; Cholewa *et al.*, 2007; Kohn *et al.*, 2007; Rack *et al.*, 2010), and even with specific laboratory sources (Tuohimaa *et al.*, 2007; Boone *et al.*, 2009).

2. Theory

In this section we give a short synopsis of the algorithm used by ANKPhase and first published by Paganin *et al.* (2002). We also outline technical aspects related to the implementation.

2.1. The phase reconstruction algorithm

Although in practice applicable over a wide parameter range, and in particular for polychromatic radiation and partially coherent illumination, the algorithm is derived based on the following assumptions:

- The object imaged consists of a single, homogeneous material.
- Monochromatic radiation is used.
- The incident wave is a plane wave or only mildly curved.
- The distance z between the object and the detector plane fulfils the near-field condition, *i. e.*,

$$z \ll d^2/\lambda, \quad (1)$$

where d is the characteristic size of the smallest discernible features in the object, and λ is the X-ray wavelength. If these conditions are met, the intensity distribution $I(x, y)$ measured at a single, known distance z between the object and the detector plane can be used to retrieve the projected thickness $t(x, y)$ of the object (or, which is equivalent, the projected phase shift of the X-ray wavefront) using the relation

$$t(x, y) = -\frac{1}{\mu} \ln \left(\mathcal{F}^{-1} \left[\frac{\mathcal{F}[I(x, y)/I_0(x, y)]}{1 + z\delta\mu^{-1}\sqrt{u^2 + v^2}} \right] \right). \quad (2)$$

Here, x and y are the Cartesian coordinates in the image and/or object plane, μ is the linear attenuation coefficient of the object material, \mathcal{F} and \mathcal{F}^{-1} are, respectively, the forward and backward Fourier transform operators, $I(x, y)$ is the intensity distribution in the phase-contrast radiograph, $I_0(x, y)$ is the incident intensity with-

out object at the position the detector, δ is the decrement from unity of the X-ray refractive index of the object material, u, v are the complex conjugate coordinates of x and y , and z is the object-detector distance. The quantities δ and μ are related to the complex-valued X-ray refractive index n by

$$n = 1 - \delta + i\beta \quad , \quad (3)$$

with $i^2 = -1$ and $\mu = 4\pi\beta/\lambda$. Both β and δ are dimensionless real numbers.

2.2. Flatfield and darkfield correction

In a real X-ray imaging system, the background signal (*i. e.*, signal recorded if no object is in the beam) is generally not uniform. This can be due to inhomogeneities in the X-ray beam intensity distribution or to non-uniform detector response (caused, for example, by vignetting or varying pixel sensitivities), or both. It is therefore generally necessary to normalize each radiograph by an image of the beam without the object. This is called a flatfield correction. Also, in each image recorded with the detector, the offset signal recorded when no photons hit the detector (dark signal) should be subtracted from the image before further processing (darkfield correction). The corrected images are

$$I_c(x, y) = \frac{I(x, y)}{I_0(x, y)} = \frac{S_o(x, y) - S_d(x, y)}{S_f(x, y) - S_d(x, y)} \quad , \quad (4)$$

where $S_o(x, y)$ is the image signal measured with the object in the beam, $S_d(x, y)$ is the dark signal, and $S_f(x, y)$ the flat signal (*i. e.*, the image with the sample removed). In order to keep the increase of statistical noise introduced by the correction to a minimum, it is preferable to take a series of flatfield and dark images and average these before using them for correcting the object images. ANKAphase can perform flatfield and dark-image correction of the radiographs. It can process series of flatfield images, as well as series of dark images by calculating, for every pixel, the average gray value for that pixel, where the averaging is done over all images in the series (but

separately for each pixel). In doing this, ANKAphase uses median averaging (rather than the arithmetic mean).

2.3. Boundary treatment

To avoid crosstalk between opposed ends of the images the recorded projections have to be padded to larger size before applying the phase retrieval algorithm. Without padding, crosstalk occurs because the convolution of the projection data with a phase-reconstruction kernel is carried out in Fourier space, so that the convolution is periodic. Furthermore, padding is required because the fast Fourier transform (FFT) routine used requires the number of pixels in each dimension to be a power of two.

The images are therefore padded in a two-stage approach. First, the original image with dimensions (n_x, n_y) is extended by a margin on all four sides (upper, left, right) of width

$$n_{\text{margin}} = \left\lceil \frac{3\lambda z}{(\Delta x)^2} \right\rceil. \quad (5)$$

Here, Δx is the effective pixel size of the detector, z the propagation distance and λ the X-ray wavelength. The expression $\lceil \dots \rceil$ denotes the ceiling operation, which yields the smallest integer number that is equal to or greater than the argument.

In a second step, the image with the new dimensions (n'_x, n'_y) , where $n'_i = n_i + 2n_{\text{margin}}$, is further padded so that finally both dimensions are power of two. Each pixel in the padded area is filled with the value of the nearest pixel in the original image. The final dimensions of the image are thus $n''_i = \exp\{(\ln 2)\lceil \log_2 n'_i \rceil\}$.

Equation (5) is based on the fact that a point-like feature located near the border of the input image will create a diffraction pattern consisting of a series of concentric bright and dark rings. Similar to a zone plate, the width of the outer rings decreases with their distance to the center of the pattern. Using a detector with a given pixel size Δx , the details of the diffraction pattern cannot be resolved anymore if adjacent

bright fringes are spaced by less than the size of a pixel. The additional factor of 3 excludes remaining aliasing effects. A detailed derivation of equation 5 is given in appendix A.

3. Implementation

ANKAphase is written in Java (Java Consortium, 2010). It can be run as plugin to the the widely-used scientific image processing program ImageJ (National Institutes of Health, 2010b) or as a standalone application, *i. e.*, without ImageJ running or even installed. The use of Java as the programming language ensures that the executable program file in the distribution will run on most or all hardware and software platforms for which the Java Runtime Environment is available. On computers with multiple central processing units (CPUs) or with a CPU with multiple cores, images are processed using multi-threading, which speeds calculations up by parallelizing certain tasks.

The graphical user interface is based on the Java packet “Swing”, again to ensure platform independence. All image processing routines as well as input and output functions are based on the ImageJ library *ij.jar* (National Institutes of Health, 2010b). All calculations are performed in double-precision floating-point arithmetic (8 bytes per pixel). The output files contain, depending on the user’s choice, integer data of variable bit depth or single-precision float data. The basic concept of the ANKAphase software is displayed as a flow process chart in Fig. 1.

4. User interface

A screenshot of ANKAphase running as an ImageJ plugin under Microsoft Windows XP is shown in Fig. 2. The control elements are identical on other platforms and operating systems. All parameters are accessible in a single control window. Parameter

names were chosen according to conventions in use at imaging stations of synchrotron light sources. Therefore, most synchrotron users should be able to handle ANKAphase with only minor training effort.

ANKAphase identifies the input image files it will process by the directory in which these files are located. For a given set of images taken under the same experimental conditions and with the same image dimensions for all frames, it expects all the projection radiographs to be in one directory, while the series of dark images to be averaged for the darkfield correction are supposed to be in another directory.

For the flatfield images, ANKAphase foresees two directories: one in which flat images taken before the acquisition of the projections are stored, and another in which flats taken after the acquisition of the projections are stored. If two blocks of flatfield images obtained in this manner are available, ANKAphase will correct the first half of the projection images using the first set of flatfield images, and the second half of the projections will be corrected using the second set of flatfield images. Interpolation between the two is available as an option.

It is the user's responsibility to ensure that the dimensions and data type of all image files in the input directories are the same. Leaving other files in the corresponding directory will prevent ANKAphase from starting to work.

A detailed view of the graphical user interface of ANKAphase is shown in Fig. 3. The paths to the files containing the raw data can be entered directly or chosen *via* the file selection dialog of the operating system. Optional functionality can be turned on and off through check boxes. In this way, ANKAphase offers flexibility and can, for example, even be used to perform only flatfield correction.

ANKAphase recognizes the following file formats, by their file-name extension: TIFF (8-bit unsigned integer, 16-bit unsigned integer and 32-bit single precision float format), JPEG (8-bit unsigned integer), PNG (8-bit unsigned integer), BMP (8-bit

unsigned integer) and the ESRF specific data format EDF (32-bit single precision float format) (ESRF, 2010). ANKAphase preferably writes output files containing the results in single precision float format. However, if desired by the user, the results can also be written out in integer-type data formats. If a file format with an integer data type is selected, the corresponding parameters for the data reduction (re-scaling and cropping of saturated values) can be entered manually or determined automatically by ANKAphase *via* the individual minimum and maximum values for each calculated image or the first projection image only.

A standard procedure for processing a set of projections with ANKAphase consists of entering the required paths as well as the experimental parameters and activating the flatfield and the phase-retrieval option. Tools to calculate δ and β from the stoichiometry and the density of the sample material are available online (Center for X-Ray Optics, 2010) or for download (Sanchez del Rio & Dejus, 1998). It is recommended to calculate in a first step only one phase map together with the corresponding flatfield-corrected projection. If the parameters chosen are appropriate, ANKAphase should have calculated from the flatfield-corrected fringe image a phase map which should be nearly void of fringes, cf. Fig.4. Users should keep in mind that the algorithm is suited for quasi-homogeneous objects only, *i. e.* for objects in which the ratio of δ and β is rather constant and only the density changes. Phase retrieval of an image showing, *e. g.*, an object made of metal and one made of polymer will not yield a fringe-free phase map. Once the parameters are set, the full set of projection images can be processed. The number of CPUs used in parallel can be selected by the user. Memory consumption has to be kept in mind (ANKAphase will stop processing with an error message when it cannot allocate enough memory).

A few technical remarks: frequently, tomographic scans are saved as file series with a fixed filename prefix combined with continuous numbering that includes flat and

dark images. It may be undesirable to move these files physically into different directories as would be required by ANKAphase. On Unix-like operating systems, a simple workaround is to create the folders needed for ANKAphase and to fill them with symbolic links pointing towards the corresponding files. If flatfield images were taken not only at the beginning and the end of a scan but as well in between, series of folders have to be used. For such cases, ANKAphase has an optional parameter named “Output file start number” that allows to create continuously numbered files containing the phase maps. Once processing is launched, a file containing settings will be stored in the output folder. It can later be used to re-load the applied parameters. More technical details can be found in appendix B and in the ANKAphase user guide included in the distribution.

5. Examples

In this section, selected examples of phase retrieval applications based on the use of ANKAphase are shown. While they cover only a small area of the diverse scientific fields where phase-sensitive X-ray imaging is beneficial, the examples underline the strength of the algorithm as it can be applied on arbitrarily absorbing samples, in a quantitative manner as well as on projections acquired using polychromatic radiation.

5.1. Quantitative phase retrieval

In case all of the conditions concerning illumination and sample as listed in section 2.1 are fulfilled, equation (2) will yield the projected thickness $t(x,y)$ of the imaged objects (equivalent to the projected phase shift of the X-ray wavefront). In order to verify the implementation of ANKAphase, a glass capillary was chosen as a simple arbitrarily absorbing specimen and imaged with monochromatic X-rays.

In Fig. 4 (top) a flat- and dark-corrected radiograph of this object is shown, obtained

with the microimaging setup at the beamline ID22 of the European Synchrotron Radiation Facility (ESRF) (Weitkamp *et al.*, 1999). 17-keV radiation from a Si(111) double-crystal monochromator (DCM) was used; the relative spectral bandwidth of the radiation from the DCM is on the order of $\Delta E/E \approx 10^{-4}$.

For this and all of the following examples, high-resolution detection of the X-ray images was ensured by a lens-coupled system based on a scintillator screen and a digital image sensor based on a charge-coupled device (CCD), *i. e.*, by an indirect detection scheme in which the X-ray intensity distribution is first converted to a visible-light image that is then magnified and projected onto a digital sensor with a microscope. This scheme was developed during the 1990s (Bonse & Busch, 1996; Koch *et al.*, 1998), shortly after scientific-grade CCDs had become affordable. Today such optical systems can be bought from commercial suppliers such as Optique Peter, Lyon, France, although high-resolution scintillator screens of high quality remain difficult to obtain and often still require additional dedicated development by the laboratories (Martin & Koch, 2006; Martin *et al.*, 2009; Douissard *et al.*, 2010).

For the example in this section, the scintillator was a 6.2- μm -thick GGG:Eu (Eu-doped $\text{Gd}_3\text{Ga}_5\text{O}_{12}$) single crystal grown on top of an undoped GGG substrate. It was positioned 15 mm away from the sample. The light from the scintillator was projected onto the chip of a FReLoN 2000 camera by a microscope optic consisting of a $10\times/\text{NA } 0.4$ objective and a $2\times$ eye-piece (Labiche *et al.*, 2007; Martin & Koch, 2006). Since the CCD pixels have a size of 14 μm , the effective pixel size with which the image was sampled was 0.7 μm . The spatial resolution of this detector configuration was around 2 μm (verified with an X-ray test pattern by Xradia, type X-500-200-30).

For the phase-retrieval, values of β and δ corresponding to SiO_2 (2.4 g/cm³) were used, obtained from the DABAX database (Sanchez del Rio & Dejus, 1998). The calculated phase map is shown in Fig. 4 (middle). With the inner and outer capil-

lary radii known, the projected thickness of the object can be calculated as well. A combined plot showing the measured projected thickness and the theoretical one are shown in Fig. 4 (bottom). The agreement between experimental data and theoretical calculations is remarkable.

5.2. Materials Research

The example shown in this section has a two-fold function as it stands for materials research as well as for an object where little *a priori* information about the exact constituents inside was available: a sample of recycled paper (kindly provided by the Papiertechnische Stiftung PTS, Munich, Germany). The microstructure of paper determines important mechanical properties such as its tensile strength or filtration properties. Therefore, paper microstructure has been studied for a long time, yet mainly based on two-dimensional imaging techniques such as scanning electron microscopy. For the study shown here, an X-ray microtomography data set was acquired in a “local tomography” geometry (with the sample size exceeding the field of view of the detector), again using the microtomography stage at ID22 of the ESRF with monochromatic radiation from the crystal monochromator of this beamline. The X-ray photon energy for this study was 13 keV. The pixel size of the detector was 0.35 μm , obtained through a 20 \times objective (NA 0.7) and a 2 \times eyepiece that projected the image from the 3.5- μm -thin LAG:EU (Eu-doped $\text{Lu}_3\text{Al}_5\text{O}_{12}$) scintillator crystal onto the CCD detector with 14 μm pixel size (Koch *et al.*, 1999). The spatial resolution of this detector configuration was around 1 μm (verified again with an X-ray test pattern by Xradia, type X-500-200-30).

The tomographic reconstruction was carried out using filtered backprojection (Kak & Slaney, 1988) *via* the PyHST software package (Mirone *et al.*, 2010).

An example slice reconstructed without prior phase retrieval or other further pro-

cessing, showing edge-enhancing X-ray inline phase contrast, is displayed in Fig. 5 (top, left). Most of the cellulose fibres are collapsed. This causes the microstructure to be very irregular. The same data set was then reconstructed using projections to which phase retrieval with ANKAphase had been applied. The initial parameters for phase retrieval were estimated *via* the CXRO online calculator (Center for X-Ray Optics, 2010) and then optimised manually to obtain images that facilitate interpretation and segmentation in an optimal way. A tomographic slice corresponding to the one shown in the top left panel of Fig. 5, but reconstructed after phase retrieval, is depicted in the top right panel of the same figure. Besides the increased contrast between the specimen and the background, different additives contained in the paper can now be distinguished. A volume rendering of the segmented tomographic volume reconstructed from the phase-retrieved projections is shown in Fig. 5 (bottom). The multi-constituent data set reveals the additives as well as information on the cellulose fiber structure. For the separation, Boolean volume images were created *via* an algorithm based on region-growing in combination with a threshold hysteresis (Rack *et al.*, 2008a). Further details about volume analysis tasks that are relevant for this type of data can be found in the literature (Antoine *et al.*, 2002; Ohser *et al.*, 2009).

5.3. Life Sciences

The example data shown in this section was acquired as part of a study in which the morphology of different mosquitoes (genus *Anopheles*) had to be compared. It demonstrates that even when polychromatic radiation – here, a filtered white beam from a bending magnet – is used to illuminate the sample, the algorithm used by ANKAphase can deliver images of high quality in terms of spatial resolution and contrast.

The experiments were carried out at the ANKA light source of the Karlsruhe Insti-

tute of Technology (KIT, formerly Forschungszentrum Karlsruhe), Germany, in collaboration with the Entomology Unit and the X-ray Laboratories of the International Atomic Energy Agency (IAEA Laboratories, Seibersdorf, Austria) and the Atominstitut of the Technische Universität Wien (Vienna, Austria). The advantage of phase-sensitive X-ray imaging here is that it allows for probing a sample characterised by very weak or no absorption contrast. This is generally of interest for radiography of soft tissue, small animals, and insects, where the available material thickness is not sufficient to produce satisfactory absorption contrast. Another advantage over X ray absorption radiography can be minimization of the radiation dose to the sample. The technique allows the investigation of live animals or the performance of tomographic imaging with longer exposure time with minimum radiation damage to the otherwise sensitive and delicate samples (Betz *et al.*, 2007; Socha *et al.*, 2007; Westneat *et al.*, 2008; Rack *et al.*, 2010).

The tomographic scans were performed at the bending-magnet beamline TopoTomo of ANKA (Rack *et al.*, 2009b). A white beam from the bending magnet was used, spectrally filtered only by a 0.5-mm-thick beryllium window, a silicon wafer of 1 mm thickness, and approximately 1.5 m of air path. The resulting energy spectrum has its maximum around 20 keV with a bandwidth $\Delta E/E$ of approximately 75%. The image detector consisted of a 25- μm -thick LuAG:Eu scintillator (grown on a 160- μm YAG substrate), a $4\times/\text{NA } 0.16$ microscope objective and $2.5\times$ eyepiece, and an “off-the-shelf” CCD-based camera with an array of 4008×2672 pixels of 9 μm size (PCO, Germany, model pco.4000). The detector thus operated with an effective pixel size of 0.9 μm . A glass filter (type FGL 495, Schott, Germany) was inserted into the optical beam path of the microscope in order to block parasitic luminescence from the YAG substrate (Rack *et al.*, 2008b), which would otherwise have degraded spatial resolution. The resulting resolution was experimentally determined with an X-ray test pattern

(Xradia, type X-500-200-30) to be approximately 2.5 μm (Rack *et al.*, 2009b).

The sample-detector distance was approximately 50 mm. 1000 projection images of the chemically fixed specimen were taken during rotation over a range of 180 degrees. Here as in the previous examples, standard filtered back-projection tomographic reconstruction using the software package PyHST was employed.

In Fig. 6 (top, left) an example radiograph of a mosquito head can be seen, dominated by X-ray inline phase contrast. In the same figure, the corresponding tomographic reconstruction of an example slice without phase reconstruction is depicted (bottom, left). Various detailed features can be distinguished due to edge enhancement, but the contrast between foreground and background remains poor. For the phase reconstruction, chitin ($\text{C}_{16}\text{O}_9\text{N}_2\text{H}_{16}$) with a density of 1.4 g/cm^3 was assumed to be the dominating material in order to determine β and δ (Neville *et al.*, 1976). In order to obtain phase maps without any remaining edge enhancement, the reconstruction parameter “X-ray photon energy” was set to 18 keV, which corresponds to the mean energy as seen by the imaging detector. Furthermore, the parameter “propagation distance” had to be set to 30 mm. The corresponding results can be found in the right panel of Fig. 6. The phase retrieval introduces significant blurring, as can be seen in the radiographic projection. However, the tomographic reconstruction after phase retrieval reveals excellent contrast between foreground and background. Plain thresholding is now sufficient for segmentation, a volume rendering of the complete tomographic data set is shown in Fig. 7. Images of this kind are excellently suited to study morphological details of, *e. g.*, internal mosquito organs by entomologists.

6. Conclusions

ANKAphase has been designed to give a broader community access to phase retrieval from X-ray inline phase contrast images. To this end, a simple and robust algorithm

has been chosen that allows the retrieval of phase maps based on X-ray transmission radiographs of arbitrarily absorbing samples. The examples shown demonstrate that even if polychromatic and moderately coherent synchrotron light is used for illumination, a significant increase in the contrast between foreground and background within the tomographic images and uniform gray level contrast inside the sample material can be achieved. Through a graphical user interface, phase retrieval can be performed with ANKAphase requiring only the parameters of the experimental setup and an estimate about the constituents of the sample.

The application examples shown demonstrate the value of ANKAphase as a tool that extends the potential of tomography data dominated by X-ray inline phase contrast and acquired at a single propagation distance. It is particularly useful for applications in which subsequent volume image analysis has to be applied, frequently based on the creation of Boolean volume data (segmentation), as well as for high quality volume renderings required to study detailed morphological features in three dimensions.

Users of ANKAphase should keep in mind that the algorithm used by ANKAphase leads to a blurring of the images, as seen, for example, in Fig. 6. Hence, it does not compete with or replace more sophisticated methods such as holotomography (Cloetens *et al.*, 1999), which, on the other hand, needs data taken at several different distances between sample and detector. Blurring can be reduced by choosing shorter propagation distances than the experimentally true value when setting the phase-reconstruction parameters. This will allow some edge enhancing fringes to remain and therefore result in a sharper image. This trick comes at the cost that the resulting phase maps have no clearly-defined quantitative meaning anymore. Finally, although this may seem trivial, in order to perform quantitative phase reconstructions in three dimensions, one has to make sure that the corresponding tomographic reconstruction software used is working in a quantitative manner as well.

ANKAphase can be downloaded from the ImageJ plugin web site (National Institutes of Health, 2010a). The distribution includes a user manual in PDF and HTML format.

Appendix A

Derivation of equation 5 (Boundary treatment)

The main purpose of padding the images is to avoid crosstalk between opposed ends of the projection images, *i. e.*, avoid that features near the opposite border of the original image show up in the phase-reconstructed images.

Without edge padding, this phenomenon occurs because the convolution of the projection image with a phase-reconstruction kernel is usually carried out in Fourier space, so that the convolution is periodic.

The reconstruction kernel will generally include a backpropagation from the detector plane to the object plane. The (back-) propagation of a point-like feature in the original image, for example a feature located near the edge of the original image, will create a diffraction pattern consisting of a series of concentric bright and dark rings. With increasing distance r from the center of the pattern, the width δ_r of the rings decreases

in the same manner as the zone widths of a Fresnel zone plate, *i. e.*,¹

$$\delta_r(r) \approx \frac{\lambda z}{2r} . \quad (13)$$

Note that each of the bright and dark fringes are counted as individual rings; two adjacent bright fringes are thus separated by $2\delta_r$.

Using a detector with given pixel size Δx , the details of the diffraction pattern cannot be resolved anymore if adjacent bright fringes are spaced by less than the size of a pixel. This also implies that the diffraction pattern of a pointlike feature that is further away from the edge of the field of view than a distance r will not be resolved at the edge anymore if

$$2\delta_r(r) \lesssim \Delta x . \quad (14)$$

By adding a further factor of 3 (to exclude any remaining aliasing effects) to the requirement expressed in equation 14 and substituting r from equation (13) for r_{margin} , we get the requirement that the margin width r_{margin} should be at least

$$r_{\text{margin}} \geq \frac{3\lambda z}{\Delta x} . \quad (15)$$

¹ **Derivation of equation 13:** As known (Thompson & Vaughan, 2001), the j -th ring in a zone-plate pattern has a radius of

$$r_j = \sqrt{j\lambda z + (j\lambda/2)^2} \quad (6)$$

$$\approx \sqrt{j\lambda z} \text{ for } z \gg j\lambda . \quad (7)$$

The width of the j -th zone can be approximated by

$$\delta_{r_j} = r_{j+1} - r_j \quad (8)$$

$$= \sqrt{j\lambda z} \left(\sqrt{1 + j^{-1}} - 1 \right) \quad (9)$$

$$\approx \sqrt{j\lambda z}/(2j) \text{ (for } j \gg 1) \quad (10)$$

$$= \sqrt{\lambda z/(4j)} \quad (11)$$

$$\stackrel{(7)}{=} \lambda z/(2r_j) . \quad (12)$$

Note that we assumed $1 \ll j \ll (z/\lambda)$ in this derivation. Substituting equation (7) for j , we see that this assumption is equivalent to $\lambda z \ll r^2 \ll z^2$. In practice, these assumptions will always be fulfilled. This can be seen by substituting r with r_{margin} from equation (15), which yields $3\sqrt{\lambda z} \gg \Delta x \gg 3\lambda$ as another equivalent expression of the assumption. The first condition $\sqrt{\lambda z} \gg \Delta x$ is fulfilled because if the pixel size Δx were not much smaller than the first Fresnel zone width $\sqrt{\lambda z}$, inline phase contrast could not be resolved in the first place. The second condition $\Delta x \gg 3\lambda$ is met even more obviously because the pixel size will always be very much larger than the X-ray wavelength.

Since the margin width in units of pixels, n_{margin} , is related to the width r_{margin} expressed in length units by $n_{\text{margin}} = r_{\text{margin}}/\Delta x$, the equation above is equivalent to equation 5.

Appendix B

Hardware and software requirements

B.1. Platforms and operating systems

ANKAphase being written in Java, it should run on any platform and with any operating system for which Java is available, including Microsoft Windows, Mac OS, and GNU/Linux systems. However, the program has so far been tested only on Microsoft Windows XP and Vista, SuSE Linux, Ubuntu and Redhat as well as Mac OS Snow Leopard systems.

B.2. Software requirements

In order to run ANKAphase, the Java Runtime Environment (JRE) is required, version 1.6 (*i. e.*, Java SE 6) or higher. JRE is available free of charge from Sun Microsystems (Java Consortium, 2010). ANKAphase can be used as a plugin for ImageJ. In order to do so, ImageJ needs to be installed on the system. Like ANKAphase, ImageJ is programmed in Java. However, ANKAphase does not need ImageJ to be installed and will run as a standalone application too.

Acknowledgements

The following persons contributed to the success of the experiments and supported the development of ANKAphase in general: N. Zoeger, C. Streli, P. Wobrauschek (TU

000
001
002
003
004
005
006
007
008
009
010
011
012
013
014
015
016
017
018
019
020
021
022
023
024
025
026
027
028
029
030
031
032
033
034
035
036
037
038
039
040
041
042
043
044
045
046
047
048
049
050
051
052
053
054
055
056
057
058
059
060
061
062
063
064
065
066
067
068
069
070
071
072
073
074

Wien), A. Markowicz, E. Chinea-Cano (IAEA), A. Cecilia, T. dos Santos Rolo, T.
Rack (ANKA), K. Sandau and J. Ohser (Hochschule Darmstadt).

REVIEW DOCUMENT

References

- Antoine, C., Nygård, P., Gregersen, Ø. W., Holmstad, R., Weitkamp, T. & Rau, C. (2002). *Nucl. Instr. & Meth. in Phys. Res. A*, **490**(1-2), 392–402.
- Banhart, J. (ed.) (2008). *Advanced Tomographic Methods in Materials Research and Engineering*. Oxford University Press.
- Betz, O., Wegst, U., Weide, D., Heethoff, M., Helfen, L., Lee, W. & Cloetens, P. (2007). *J. Microsc.* **227**(1), 51–71.
- Bonse, U. & Busch, F. (1996). *Prog. Biophys. Molec. Biol.* **65**, 133–169.
- Boone, M., Witte, Y. D., Dierick, M., den Bulcke, J. V., Vlassenbroeck, J. & Hoorebeke, L. V. (2009). *Nucl. Instr. Meth. B*, **267**(7), 1182–1186.
- Bronnikov, A. V. (2002). *J. Opt. Soc. Am. A*, **19**, 472–480.
- Brun, F., Mancini, L., Kasae, P., Favretto, S., Dreossi, D. & Tromba, G. (2010). *Nucl. Instr. & Meth. in Phys. Res. A*, **615**(3), 326–332.
- Center for X-Ray Optics, (2010). CXRO web site. <http://www-cxro.lbl.gov/>.
- Cholewa, M., Ping, Y., Ling, N. M., Juan, L. Z., Moser, H. O., Hwu, Y. & Gureyev, T. E. (2007). *Nucl. Instr. & Meth. in Phys. Res. B*, **260**(1), 45–48.
- Cloetens, P., Barrett, R., Baruchel, J., Guigay, J.-P. & Schlenker, M. (1996). *J. phys. D, Appl. phys.* **29**(1), 133–146.
- Cloetens, P., Ludwig, W., Baruchel, J., Dyck, D. V., Landuyt, J., Guigay, J. P. & Schlenker, M. (1999). *Appl. Phys. Lett.* **75**, 2912–2914.
- Denecke, M. A., de Nolf, W., Rack, A., Tucoulou, R., Cloetens, P., Vitova, T., Falkenberg, G., Abolhassani, S. & Kienzler, B. (2011). *Actinide Nanoparticle Research*, chap. Speciation of actinides in granite subjected to tracer studies, p. in print. Springer, Berlin; Heidelberg.
- Douissard, P.-A., Cecilia, A., Martin, T., Chevalier, V., Couchaud, M., Baumbach, T., Dupré, K., Kühbacher, M. & Rack, A. (2010). *J. Synchrotron Radiat.* **17**(5), 571–583.
- ESRF, (2010). Implementation of the EDF Data Format in the SAXS Package. <http://www.esrf.eu/UsersAndScience/Experiments/TBS/SciSoft/OurSoftware/SAXS/SaxsHeader>.
- Graeff, W. & Engelke, K. (1991). In *Handbook on Synchrotron Radiation*, edited by S. Ebashi, M. Koch & E. Rubenstein, vol. 4, pp. 361–406. North-Holland; Amsterdam, Oxford, New York, Tokyo.
- Groso, A., Abela, R. & Stampanoni, M. (2006). *Opt. Express*, **14**(18), 8103–8110.
URL: <http://www.opticsexpress.org/abstract.cfm?URI=oe-14-18-8103>
- Gureyev, T. E., Raven, C., Snigirev, A., Snigireva, I. & Wilkins, S. W. (1999). *J. Phys. D*, **32**, 563–567.
- Gureyev, T. E., Stevenson, A. W., Paganin, D. M., Weitkamp, T., Snigirev, A., Snigireva, I. & Wilkins, S. C. (2002). *J. Synchrotron Rad.* **9**, 148–153.
- Java Consortium, (2010). The Java Web Site. <http://www.java.com/>.
- Kak, A. C. & Slaney, M. (1988). *Principles of Computerized Tomographic Imaging*. IEEE Press, New York.
- Koch, A., Peyrin, F., Heurtier, P., Ferrand, B., Chambaz, B., Ludwig, W. & Couchaud, M. (1999). In *Physics of Medical Imaging*, edited by J. M. Boone & J. T. Dobbins III, vol. 3659 of *Proc. of SPIE*, pp. 170–179.
- Koch, A., Raven, C., Spanne, P. & Snigirev, A. (1998). *J. Opt. Soc. Am. A*, **15**, 1940–1951.
- Kohn, V. G. (1997). *Physica Scripta*, **56**, 14–19.
- Kohn, V. G., Argunova, T. S. & Je, J. H. (2007). *Appl. Phys. Lett.* **91**(17), 171901.
- Labiche, J.-C., Mathon, O., Pascarelli, S., Newton, M. A., Ferre, G. G., Curfs, C., Vaughan, G., Homs, A. & Carreiras, D. F. (2007). *Rev. Sci. Instrum.* **78**, 0901301.
- Langer, M., Cloetens, P., Guigay, J.-P. & Peyrin, F. (2008). *Med. Phys.* **35**(10), 4556–4566.
- Maleki, M. H. & Devaney, A. J. (1994). *Opt. Eng.* **33**, 3243–3253.
- Manke, I., Banhart, J., Haibel, A., Rack, A., Zabler, S., Kardjilov, N., Hilger, A., Melzer, A. & Riesemeier, H. (2007). *Appl. Phys. Lett.* **90**(21), 214102.

- Martin, T., Douissard, P.-A., Couchaud, M., Cecilia, A., Baumbach, T., Dupré, K. & Rack, A. (2009). *IEEE Trans. Nucl. Sci.* **56**(3), 1412–1416.
- Martin, T. & Koch, A. (2006). *J. Synchrotron Radiat.* **13**, 180–194.
- Martín-Herrero, J. & Germain, C. (2007). *Carbon*, **45**(6), 1242–1253.
- Mayo, S. C., Chen, F. & Evans, R. (2010). *J. Struct. Biol.* **171**(2), 182–188.
- Mirone, A., Wilcke, R., Hammersley, A. & Ferrero, C., (2010). PyHST – High Speed Tomographic Reconstruction. <http://www.esrf.eu/UsersAndScience/Experiments/TBS/SciSoft/>.
- National Institutes of Health, (2010a). ImageJ ANKPhase Plugin Web Site. <http://rsbweb.nih.gov/ij/plugins/ankphase/>.
- National Institutes of Health, (2010b). The ImageJ Web Site. <http://rsb.info.nih.gov/ij/>.
- Neville, A. C., Parry, D. A. & Woodhead-Galloway, J. (1976). *J. Cell Sci.* **21**(1), 73–82.
- Nugent, K. A., Gureyev, T. E., Cookson, D. F., Paganin, D. & Barnea, Z. (1996). *Phys. Rev. Lett.* **77**, 2961–2964.
- Ohser, J., Redenbach, C. & Schladitz, K. (2009). *Image Anal. Stereol.* **28**, 179–185.
- Ohser, J. & Schladitz, K. (2009). *3D Images of Materials Structures: Processing and Analysis*. Wiley-VCH, Weinheim, Berlin.
- Paganin, D., Mayo, S. C., Gureyev, T. E., Miller, P. R. & Wilkins, S. W. (2002). *J. Microscopy*, **206**, 33–40.
- Peele, A. G., De Carlo, F., McMahon, P. J., Dhal, B. B. & Nugent, K. A. (2005). *Rev. Sci. Instrum.* **76**(8), 083707.
- Rack, A., García-Moreno, F., Schmitt, C., Betz, O., Cecilia, A., Ershov, A., Rack, T., Banhart, J. & Zabler, S. (2010). *J. X-Ray Sci. Tech.* **18**(4). In press.
- Rack, A., Helfen, L., Baumbach, T., Kirste, S., Banhart, J., Schladitz, K. & Ohser, J. (2008a). *J. Microsc.* **232**(2), 282–292.
- Rack, A., Helwig, H.-M., Büttow, A., Rueda, A., Matijašević-Lux, B., Helfen, L., Goebbels, J. & Banhart, J. (2009a). *Acta Mater.* **57**(16), 4809–4821.
- Rack, A., Weitkamp, T., Bauer Trabelsi, S., Modregger, P., Cecilia, A., dos Santos Rolo, T., Rack, T., Haas, D., Simon, R., Heldele, R., Schulz, M., Mayzel, B., Danilewsky, A. N., Waterstradt, T., Diete, W., Riesemeier, H., Müller, B. R. & Baumbach, T. (2009b). *Nucl. Instr. & Meth. in Phys. Res. B*, **267**(11), 1978–1988.
- Rack, A., Zabler, S., Müller, B., Riesemeier, H., Weidemann, G., Lange, A., Goebbels, J., Hentschel, M. & Görner, W. (2008b). *Nucl. Instr. Meth. A*, **586**(2), 327–344.
- Sanchez del Rio, M. & Dejus, R. J. (1998). In *Proceedings SPIE: Crystal and Multilayer Optics*, edited by A. T. Macrander, A. K. Freund, T. Ishikawa & D. M. Mills, vol. 3448, p. 340.
- Schelokov, I., Weitkamp, T. & Snigirev, A. (2002). *Opt. Comm.* **213**, 247–258.
- Snigirev, A., Snigireva, I., Kohn, V. & Kuznetsov, S. (1995). *Rev. Sci. Instrum.* **66**(12), 5486–5492.
- Socha, J. J. & De Carlo, F. (2008). In *Developments in X-ray Tomography VI*, edited by S. R. Stock, vol. 7078 of *Proc. of SPIE*, p. 70780A.
- Socha, J. J., Westneat, M. W., Harrison, J. F., Waters, J. S. & Lee, W.-K. (2007). *BMC Biology*, **5**(1), 6.
- Stevenson, A. W., Gureyev, T. E., Paganin, D., Wilkins, S. W., Weitkamp, T., Snigirev, A., Rau, C., Snigireva, I., Youn, H. S., Dolbnya, I. P., Yun, W., Lai, B., Garrett, R. F., Cookson, D. J., Hyodo, K. & Ando, M. (2003). *Nucl. Instrum. Meth. B*, **199**, 427–435.
- Stiller, M., Rack, A., Zabler, S., Goebbels, J., Dalügge, O., Jonscher, S. & Knabe, C. (2009). *BONE*, **44**(4), 619–628.
- Stock, S. R. (2008). *MicroComputed Tomography: Methodology and Applications*. CRC Press, London, New York, Boca Raton.
- Thompson, A. C. & Vaughan, D. (eds.) (2001). *X-ray Data Booklet*. Lawrence Berkeley National Laboratory, University of California, 2nd ed. Also available online at <http://xdb.lbl.gov>.

- Tuohimaa, T., Otendal, M. & Hertz, H. M. (2007). *Appl. Phys. Lett.* **91**(7), 074104.
- Weitkamp, T. (2002). *Imaging and Tomography with High Resolution Using Coherent Hard Synchrotron Radiation*. Cuvillier Verlag, Göttingen.
- Weitkamp, T., Raven, C. & Snigirev, A. A. (1999). In *Developments in X-ray Tomography II*, edited by U. Bonse, vol. 3772 of *Proc. of SPIE*, pp. 311–317.
- Westneat, M. W., Betz, O., Blob, R. W., Fezzaa, K., Cooper, W. J. & Lee, W.-K. (2003). *Science*, **299**, 558–560.
- Westneat, M. W., Socha, J. J. & Lee, W.-K. (2008). *Annu. Rev. Physiol.* **70**, 119–142.
- Wilkins, S. W., Gureyev, T. E., Gao, D., Pogany, A. & Stevenson, A. W. (1996). *Nature*, **384**, 335–337.
- Xu, F., Helfen, L., Moffat, A. J., Johnson, G., Sinclair, I. & Baumbach, T. (2010). *J. Synchrotron Radiat.* **17**(2), 222–226.
- Zabler, S., Rueda, A., Rack, A., Riesemeier, H., Zaslansky, P., Manke, I., Garcia-Moreno, F. & Banhart, J. (2007). *Acta Mater.* **55**(15), 5045–5055.

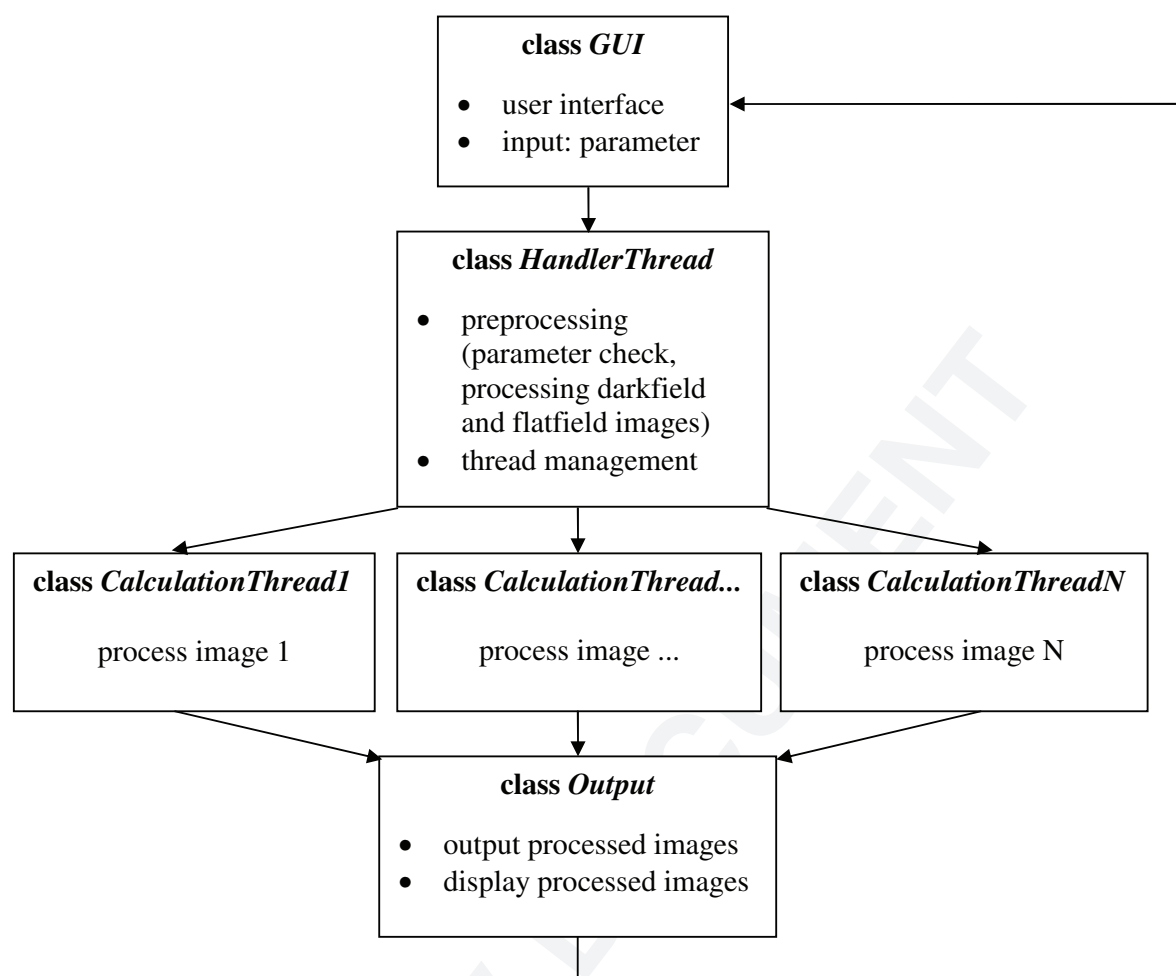


Fig. 1. [1-column-span] Flow process chart showing the basic design of the ANKPhase software as realised in Java (Java Consortium, 2010).

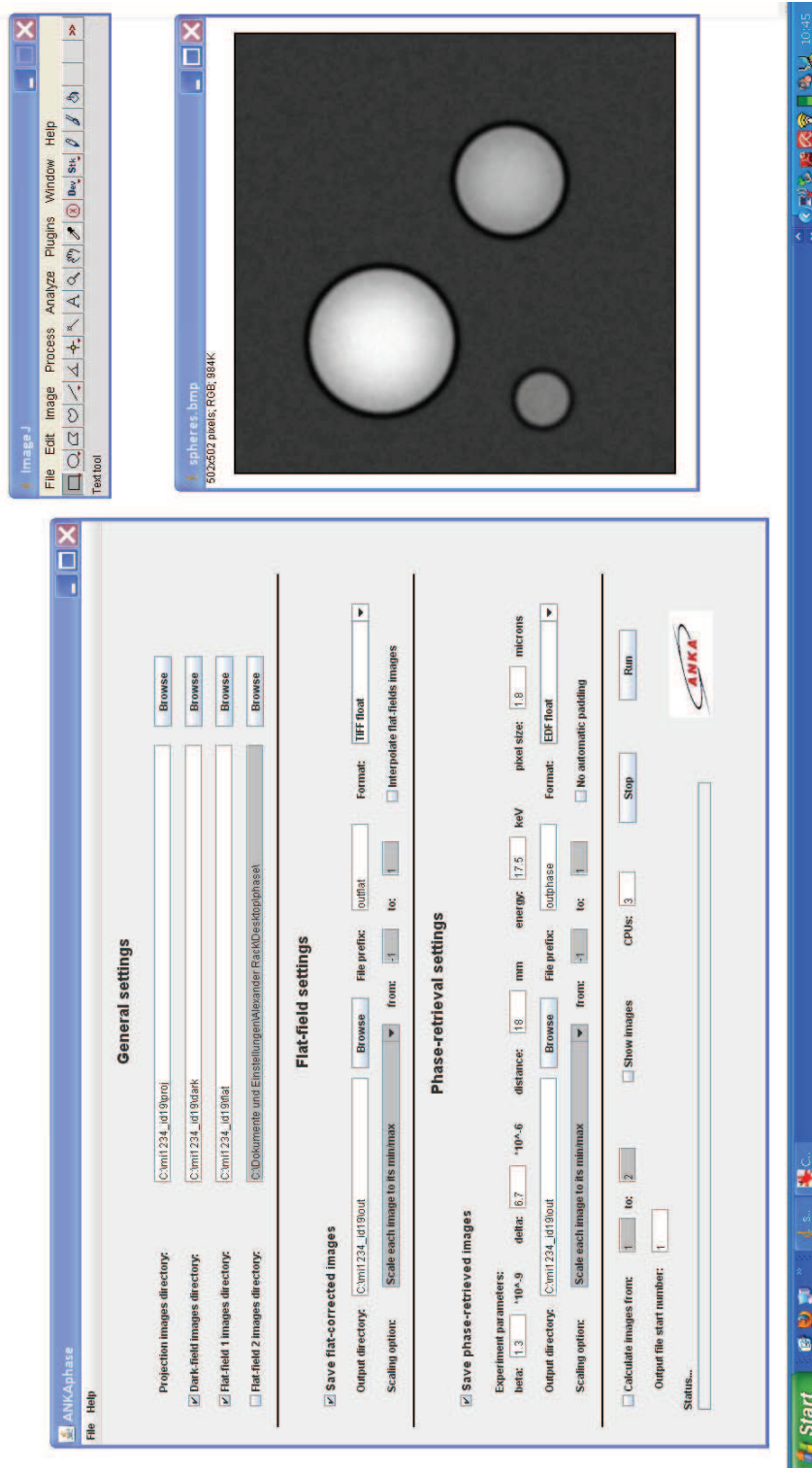


Fig. 2. [1.5-column-span] Screenshot of ANKPhase operated as ImageJ plugin under Microsoft Windows XP.

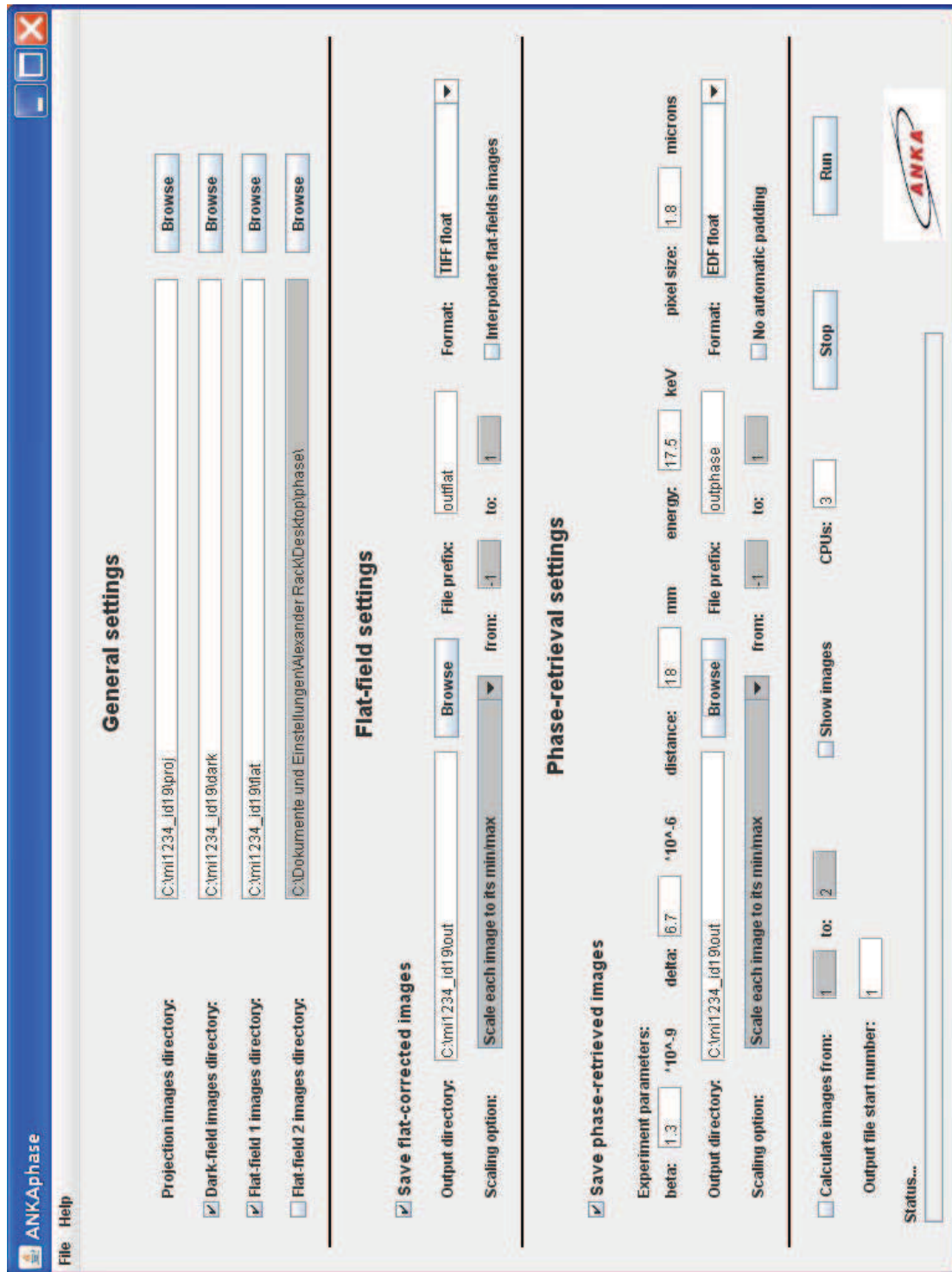


Fig. 3. [1.5-column-span] The graphical user interface of ANKPhase. All parameters can be directly accessed through a single control window.

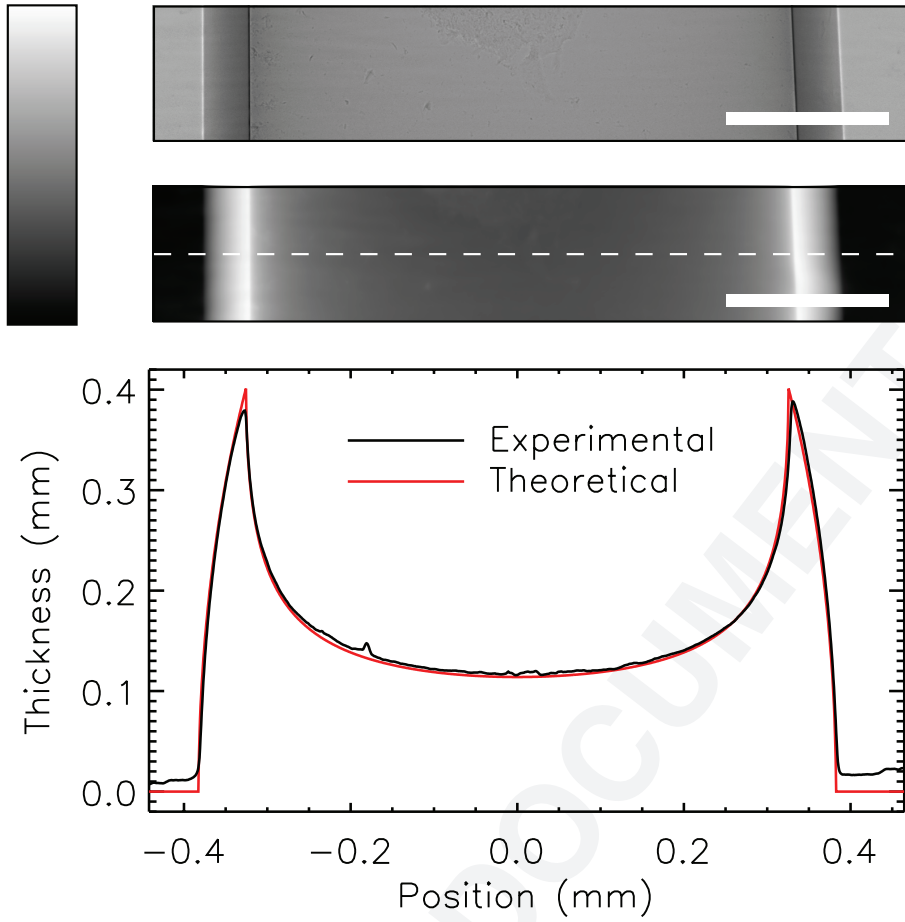


Fig. 4. [1-column-span] Quantitative phase retrieval. Top: projection radiograph of a glass capillary, taken with monochromatic X-rays of 17 keV and at a sample-detector distance of 15 mm. The image has been corrected for dark signal and flatfield-normalized. The grayscale image shows the transmission signal I/I_0 , scaled between 0.4 (black) and 1.3 (white). The length of the scale bar is 200 μm . Center: image after phase reconstruction with Paganin's formula. The gray levels represent reconstructed values of the projected glass thickness between 0 (black) and 0.4 mm (white). Bottom: section profile line through the reconstructed projection image (at the position indicated by the dashed white line in the radiograph), and expected profile (red) for a capillary of outer diameter 0.765 mm and wall thickness 57 μm . The X-ray optical properties used in the reconstruction were those from the DABAX database (Sanchez del Rio & Dejus, 1998) for SiO_2 with a density of 2.4 g/cm^3 at 17 keV: $\delta = 1.73 \cdot 10^{-6}$, $\beta = 5.01 \cdot 10^{-9}$. Data taken at ESRF-ID22 with an effective pixel size of 0.68 μm .

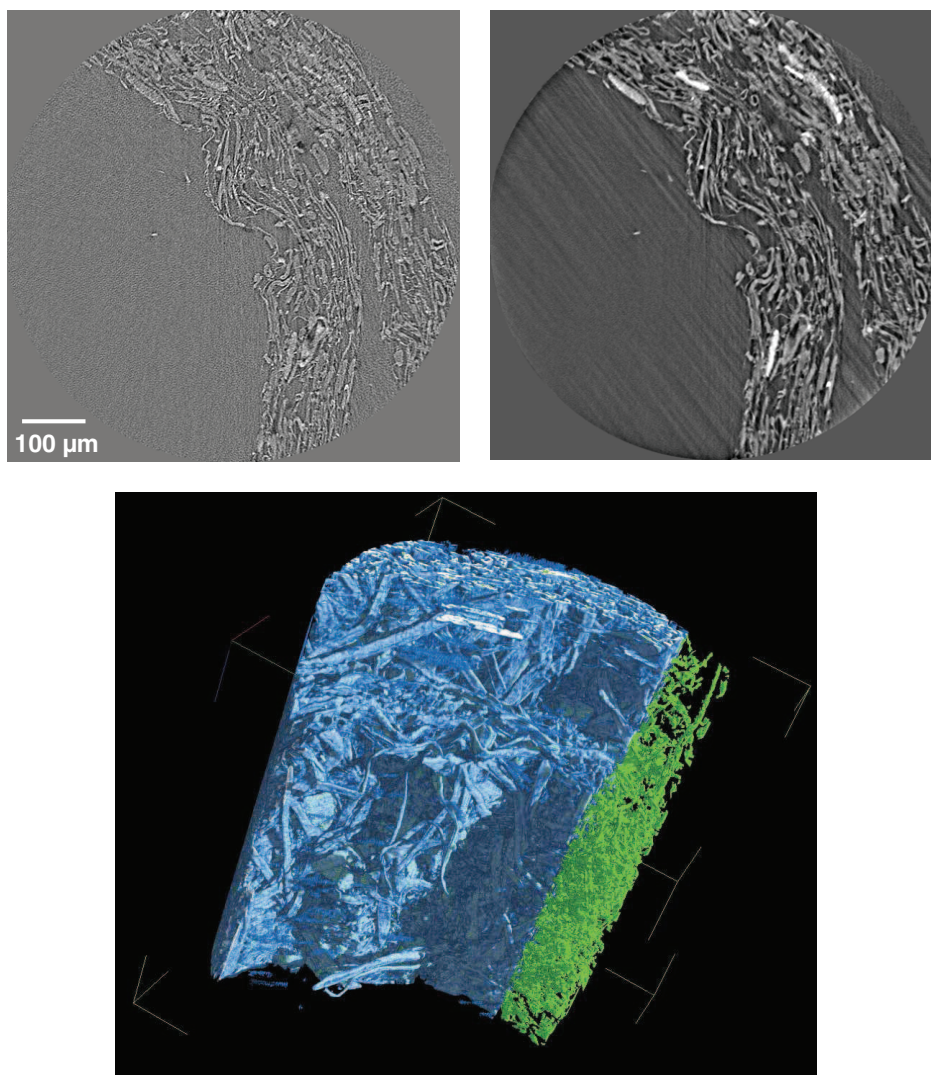


Fig. 5. [2-column-span] Microstructure of a sample of recycling paper. Top: standard reconstruction dominated by X-ray inline phase contrast (left). It is difficult if not impossible to distinguish different materials. Right: same slice reconstructed from phase-retrieved projections processed by ANKAphase. Besides the higher contrast between the sample and the background, different constituents inside the specimen can now be distinguished. The bottom image shows a volume rendering of the segmented tomographic volume data reconstructed from the phase maps. Part of the cellulose constituent (blue-white) is cropped in order visualise the additives (green).

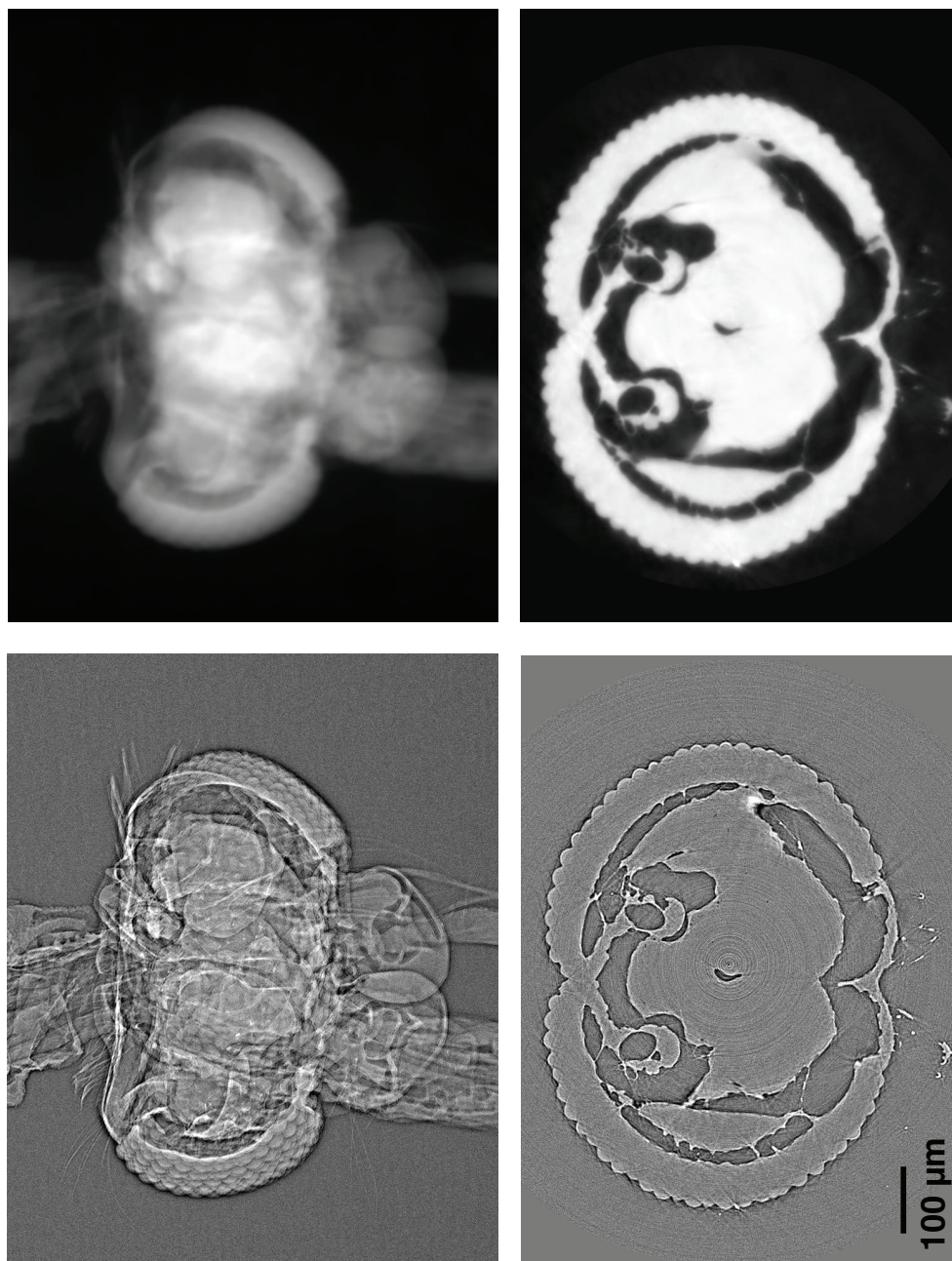


Fig. 6. [2-column-span] Head of a mosquito, imaged with filtered white beam radiation. The images in the top row show a selected radiograph dominated by X-ray inline phase contrast (left), and after phase retrieval (right). The bottom panels show the corresponding reconstructions of an example slice from the same data set. A volume rendering based on phase-retrieved tomographic image data is shown in Fig. 7.

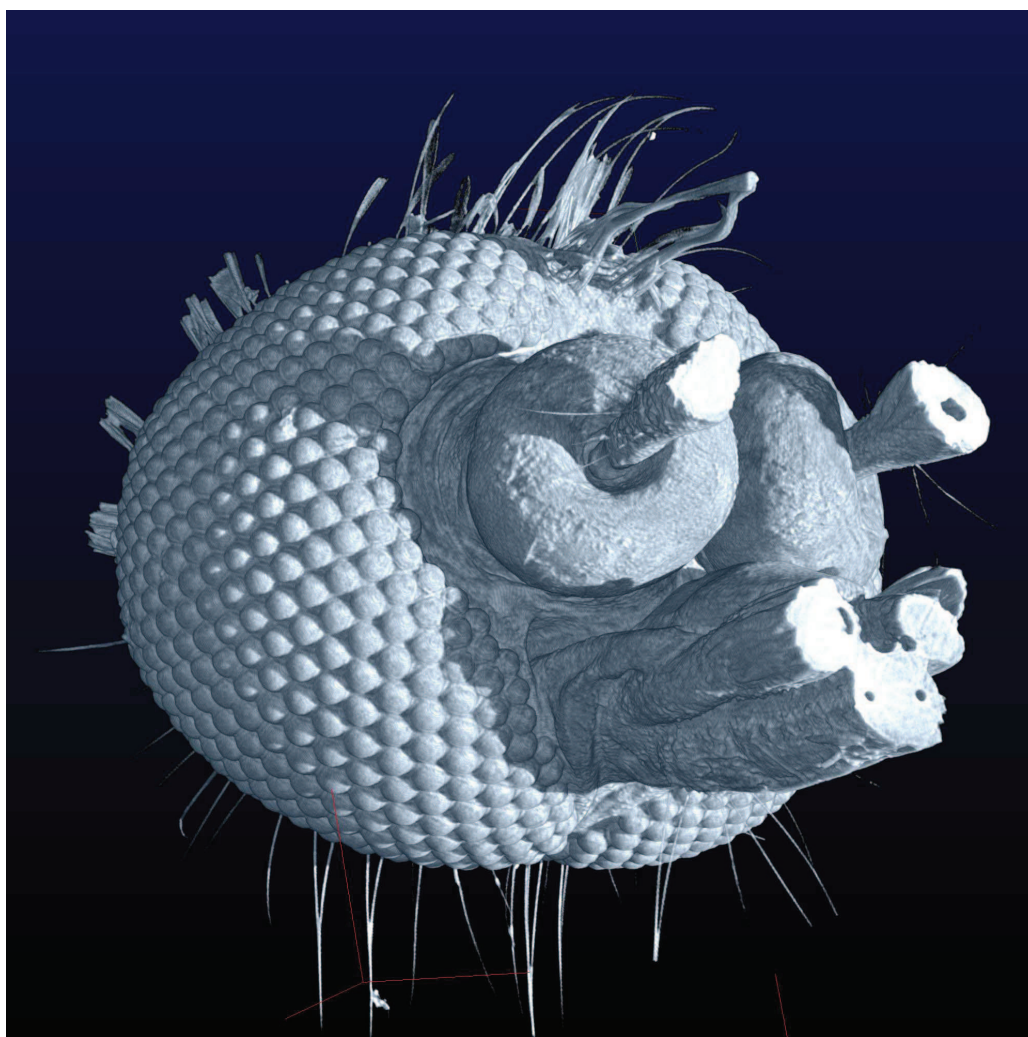


Fig. 7. [2-column-span] Volume rendering of a phase-retrieved tomographic data set showing the head of a mosquito (genus *Anopheles*), cf. Fig. 6. Volume data of this kind allow biologists to study morphological differences between individual animals or different species.

Synopsis

ANKAphase is a computer program that processes X-ray inline phase-contrast radiographs by reconstructing the projected thickness of the object(s) imaged. The program uses a single-distance non-iterative phase-retrieval algorithm described in a paper by D. Paganin *et al.* (2002).
